atmosphere

MDPI

Article

The Sensitivityof GPS Precipitable Water Vapor Jumps to Intense Precipitation Associated with Tropical Organized Convective Systems

Thamiris B. Campos [1,*], Luiz F. Sapucci [2], Cristiano Eichholz [2], Luiz A. T. Machado [3,4] and David K. Adams [5]

[1] Departamento de Ciências Atmosféricas, Instituto de Astronomia, Geofísica e Ciências Atmosféricas, Universidade de São Paulo, São Paulo 05508-090, SP, Brazil
[2] National Institute for Space Research, Center for Weather Forecasting and Climate Research, Cachoeira Paulista 12630-000, SP, Brazil
[3] Multiphase Chemistry Department, Max Planck Institute for Chemistry, 55128 Mainz, Germany
[4] Instituto de Física, Universidade de São Paulo, São Paulo 05508-090, SP, Brazil
[5] Instituto de Ciencias de la Atmósfera y Cambio Climático, Universidad Nacional Autónoma de México, Mexico City 04510, Mexico
* Correspondence: thamiris.campos@usp.br

Abstract: The Global Positioning System (GPS) consists of a constellation of satellites that transmit radio frequency signals to many users with varied applications. For meteorological purposes, the based-ground GPS receivers can provide high-quality column or precipitable water vapor (PWV), as obtained by radiosondes, but with high temporal resolution and low cost. A dense GPS network containing 16 ground-based receivers was installed in Belém city, Brazil, during the period 2–29 June 2011. This network provides a unique opportunity to evaluate the sensitivityof rapid increases in GPS PWV (GPS PWV jumps to the intense precipitation often associated with tropical organized convective systems. Results reveal a characteristic timescale of water vapor convergence before GPS-PWV maximum, which can be used for indicating the occurrence of precipitation associated with organized convective systems. A PWV increase of 4 mm h^{-1} in a period of an hour or 30 min before the maximum peak GPS-PWV (a peak of at least 57 mm) was observed during organized convection events. The contingency table obtained indicates a probability of detection of 84% and a false alarm ratio of 25% to forecast precipitation events. These results obtained suggest that GPS-PWV jumps can be employed to predict the events associated with organized convection.

Keywords: Global Positioning System (GPS); precipitable water vapor (PWV); GPS-PWV jumps; organized convective systems; forecast; precipitation

Citation: Campos, T.B.; Sapucci, L.F.; Eichholz, C.; Machado, L.A.T.; Adams, D.K. The Sensitivityof GPS Precipitable Water Vapor Jumps to Intense Precipitation Associated with Tropical Organized Convective Systems. *Atmosphere* **2023**, *14*, 262. https://doi.org/10.3390/atmos14020262

Academic Editors: Biyan Chen and Qingzhi Zhao

Received: 18 November 2022
Revised: 28 December 2022
Accepted: 29 December 2022
Published: 28 January 2023

1. Introduction

Global Positioning System (GPS) satellite constellations have been employed to estimate precipitable water vapor (PWV) for well over two decades ([1–3] and others). Many studies of atmospheric phenomena across the globe have been carried out employing GPS data which provide all-weather, high-temporal-resolution (about 5 min) PWV. Bonafoni and Riccardo 2016 [4] presented a review of a broad range of applications of both ground-based and space-based GPS receivers (radio occultation techniques) in studies of extreme weather events. Some works have used these data in data assimilation process (e.g., [5–8]). GPS PWV is employed in many observational studies for understanding and evaluating the temporal evolution of deep convective storms (e.g., [9–14]) among several different applications. With a dense GPS receivers network, the spatial distribution of the atmospheric humidity can be evaluated by tomography techniques (e.g., [15,16]) as well as the evolution of deep convection [17,18]. Of particular interest to this study is the use of GPS-PWV for nowcasting, exploring the relationship between PWV temporal variation for the forecast of intense rainfall events within a very short period of time. The use of

PWV for nowcasting has been explored using microwave radiometers, such as in the works of [19–21], or by using GPS, such as in the works of [11,22–24]. Sapucci et al. (2019) [23] introduced a new methodology exclusively using GPS data to predict the occurrence of severe storms. They explored the sharp increase in the GPS-PWV (termed by authors as "GPS-PWV jumps") before the intense precipitation, which is associated with water vapor convergence preceding the intense weather events, followed by the continued formation of cloud liquid water, as discussed by [13].

Taking into consideration the low cost of GPS receivers, relative to expensive long-term use of radiosondes, and that this technique can be used in all weather conditions, with reliable operation, this PWV monitoring methodology has several advantages. In order to further explore this application, the CHUVA Project [25] carried out a campaign in Belém, Brazil, installing a dense GPS network of 16 receivers. This campaign was performed during the period 2–29 June 2011, the squall lines season [26,27]; therefore, it was rich in organized convection events. The objective of this study is to evaluate the sensitivityof PWV jumps from a dense GPS receivers network to precipitation associated with tropical organized convective systems. Section 2 describes the dataset and the data processing algorithms used in this study. Section 3.1 identifies the organized convective systems observed during the campaign and characterizes the GPS-PWV behavior during these events. Section 3.2 investigates the GPS-PWV jumps' sensitivityto precipitation associated with organized convective systems and evaluates the technique by using a contingency table. Section 4 discusses and summarizes the main results.

2. Materials and Methods

Several field campaigns were carried out by the CHUVA Project during the period from 2010 to 2015 in different regions of Brazilian to carry out a cloud survey of the different weather regimes in Brazil [25]. The instruments installed included an X-band radar, disdrometer, precipitation gauges, radiometer, LiDAR, radiosondes, GPS receivers, and surface weather stations. The campaign carried out in Belém city was designed to study the tropical squall lines that often form along the sea-breeze front [27]. In this campaign, in addition to the typical CHUVA instrumentation, a dense GPS receivers network was installed in Belém. The objective of these additional data was to study the moisture convergence timescale associated with the shallow-to-deep convective transition as well as to observe the evolution of PWV during propagating squall line events [17]. The GPS receivers comprising this network are detailed in the next subsections.

2.1. Data Collection Strategy

Figure 1 shows the geographical location of data collection carried out during the CHUVA Project in the city of Belém, Brazil. Specifically, there are the X-band radar location and the spatial distribution of the dense GPS receivers network around the radar. More details about these receivers are presented in Table 1, such as station GPS name, acronyms (the same used in Figure 1), geographic coordinates, and meteorological station type. All GPS receivers used in this campaign are dual-frequency, TRIMBLE brand, NETR8 model, and all thee antennas are Dorne-Margolin, choke ring model. The GPS satellite signals were sampled at 1 s frequencies, whereas the respective meteorological station (see Table 1) measures the pressure and temperature every minute. The radar used in this campaign is a mobile X-band dual polarization radar (XPol), running a scan strategy with at 13 elevations, from 1° to 25°, with 1 and 150 m angular and radial resolutions, respectively, completing one volume scan every 6 min. The Belém dense GPS meteorological network covers the period from 2–29 June, in which the 16 GPS/meteorological stations were simultaneously operational.

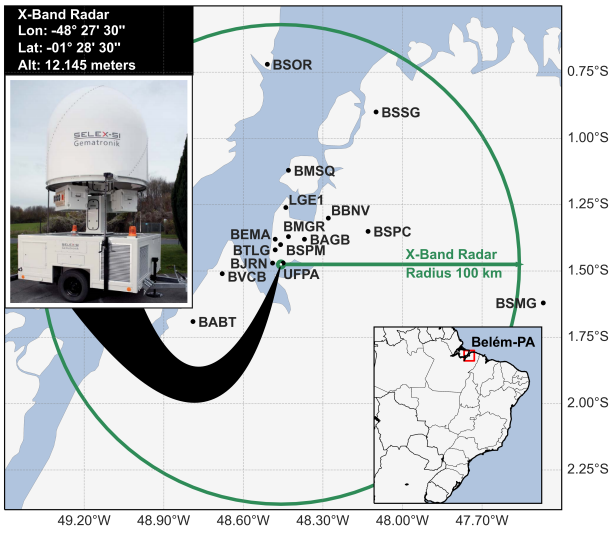

Figure 1. Geographical localization of the data collection carried out by the CHUVA Project in Belém city—Brazil. This figure shows the spatial distribution of the dense GPS network around X-band radar.

Table 1. Dense GPS receivers network installed in a campaign of data collection carried out by the CHUVA Project in Belém city during June 2011.

GPS Station Name	Acronyms	Latitude	Longitude	Altitude	Meteorological Station: Brand/Model
São Miguel do Guamá-PA	BSMG	1.62° S	47.47° W	10.97 m	Vaisala/PTU303
Telégrafo-PA	BTLG	1.4° S	48.48° W	6.27 m	Vaisala/PTU303
Santa Isabel do Pará-PA	BSPC	1.35° S	48.13° W	8.25 m	Vaisala/PTU303
Vigia-PA	BSSG	0.90° S	48.10° W	14.00 m	Vaisala/PTU303
Abaetetuba-PA	BABT	1.69° S	48.79° W	11.50 m	Vaisala/PTU303
Vila dos Cabanos-PA	BVCB	1.51° S	48.68° W	0.25 m	Vaisala/PTU303
Jurunas-PA	BJRN	1.47° S	48.49° W	3.00 m	Vaisala/PTU303
Mangeirão-PA	BMGR	1.37° S	48.43° W	3.27 m	Vaisala PTU303
Águas Brancas-PA	BAGB	1.38° S	48.37° W	5.09 m	Vaisala/PTU303
Guamá-UFPA-PA	UFPA	1.47° S	48.45° W	2.15 m	Davis
Mosqueiro-PA	BMSQ	1.12° S	48.43° W	8.75 m	Vaisala/PTU303
Soure-PA	BSOR	0.72° S	48.51° W	10.29 m	Vaisala/PTU303
SIPAM-PA	BSPM	1.40° S	48.46° W	6.37 m	Davis
DTCEA-EMA-PA	BEMA	1.38° S	48.48° W	9.83 m	Davis
Benevides-PA	BBNV	1.30° S	48.28° W	13.63 m	Davis
Outeiro-PA	LGE1	1.26° S	48.44° W	14.56 m	Vaisala/PTU303

2.2. GPS Processing Methodology

The zenith total delay (ZTD) was used to estimate the GPS-PWV values by processing the GPS data using GOA-II (Gipsy, GPS Inferred Positioning System, and OASIS, Orbit Analysis and Simulation Software II [23]) software by applying the precise point positioning method in post-processing mode. The known uncertainty sources were taken into consideration by applying the recommended models and adjusting the parameters, exploring the available stochastic models for ocean tides [28], antenna absolute calibration [29], using appropriated parameters [30], and a global mapping function [31].The sampling rate of the ZTD estimates was 5 min. More details about this data processing can be found in [23].

The zenith wet delay (ZWD) was obtained from the ZTD estimates after removing the zenith hydrostatic delay (ZHD), which was calculated from surface pressure measurement

by applying the model suggested by [32]. The zenith wet delay was converted to the PWV by using the relationship suggested by [1]:

$$PWV = ZWD\psi, \tag{1}$$

where ψ is given by the following equation:

$$\psi = \frac{10^6}{R_W[K_2' + \frac{K_3}{T_m}]} \tag{2}$$

The term R_W is the specific constant for water vapor (R_w = 461.51 J Kg^{-1} K^{-1}), K_2' and K_3 are atmospheric refractivity constants [33] , and T_m is the mean tropospheric temperature. The T_m values were obtained from the surface temperature and pressure measured at the GPS antenna by applying the regional model suggested by [34]. The sampling rate of the GPS-PWV values was 5 min.

2.3. Radar Data Processing Methodology

In order to obtain the precipitation data from the XPOL radar, the radar observation was preprocessed using the attenuation correction of the reflectivity, employing the algorithm for ground-based polarimetric radars (ZPHI algorithm) [35]. See [36] for more details on the radar preprocessing. The precipitation data from XPol radar observations were obtained by applying the dual polarization surface precipitation intensity algorithm, which calculates the precipitation rate (R) from the reflectivity (Z) and specific differential phase (K_DP) data obtained in multiple-elevation polar volumes. In this method, polarimetric measurements were used to calculate R by applying the following combined Z–R relationship [37]:

$$R = 19.63|\mathrm{K\_DP}|^{0.823} \quad for \quad Z > 35 \text{ dBZ } and \ K\_DP > 0.3^\circ \text{ km}^{-1}; \tag{3}$$

$$otherwise, \ R(Z) = (a^b)^{-1}Z^b \tag{4}$$

The CAPPI (Constant Altitude Plan Position Indicator) of 2 km was utilized to indicate the surface rain rate. The a and b values used in this equation were 200 and 1.6, respectively [38]. The final product was a rain rate (mm h^{-1} in a grid map (60 km around XPol), with a horizontal resolution of 200 m, every 6 min. There were a lot of unavailable data in this radar timescale, so to manage this problem we resampled it to a 10 min timescale, so we obtained 144 points/day (24 h × 60 min/10 min) of the surface rain rate. To analyze average precipitation in the area around the GNSS receiver, we considered total points with 200 m of horizontal resolution. For example, there were 484 points in the 4.4 km × 4.4 km area, so it was necessary to have been raining 484 mm h^{-1} in this total area, or 1 mm h^{-1} in the average area.

2.4. GOES Satellite Data

The infrared window channel (referred to as brightness temperature—BT) from the Geostationary Operational Environmental Satellite (GOES-13) was used, with a spatial resolution of 4 km × 4 km, in the sub-satellite point at 15 minute temporal resolution. BT was employed to complement the convective activity description. A brightness temperature threshold of 235 K was used to identify convective clouds [39].

2.5. The GPS Station Selection to Study the Organized Convection Events

Firstly, we characterized the organized convective systems using the GOES satellite, radar, wind profiles, and thermodynamic indices. Then, we selected the GPS/meteorological stations that are more influenced during the passage of the organized convective systems. In order to analyze the GPS-PWV time derivation, during these events, two nearly perpendicular transects were constructed, following a similar methodology to that em-

ployed by [17]. The transects were defined to capture the propagation features of the mesoscale convective system. Figure 1 shows the transects; the first one was northwest–southeast, crossing the BSOR–BMSQ–BSPC GPS stations, and the second transect was northeast–southwest, crossing the GPS stations BSSG–LGE1–BAGB–BTLG–BJRN–BABT. These 9 GPS/meteorological stations (Table 1) were used to compute the GPS jump during these two preferential directions of displacement of the organized convective systems. These transects were also chosen due to the low number of missing data from 1–30 June and being within the range of high-quality radar data.

We adopted a strategy based on surface pressure increases and temperature drop to capture the moment that organized convective systems cross the GPS station [40,41]. A convective system with at least one pixel with a reflectivity larger than 30 dBZ was considered to start the selection process of the GPS station. Fulfilling the first criterion, the time of convective system reaching the region was when surface pressure increase and temperature drop occurred until the passage moment; the pressure increase and temperature drop should be larger than +1 hPa in 20 min and −1 K in 30 min. Among the 9 GPS/meteorological stations (BSOR, BMSQ, BSPC, BSSG, LGE1, BAGB, BTLG, BJRN, and BABT), we selected those that showed the largest values of pressure increase and temperature drop (Table 2).

Table 2. Ground-based GPSaffected by organized convective systems.

Days	Ground-Based GPS
7	LGE1, BSPC, BTLG, BJRN, and BAGB
24	BTLG, BMSQ, BSSG, BJRN, and BAGB
13	BTLG, BMSQ, BSPC, BJRN, and BAGB
14	BTLG, BMSQ, BABT, BSPC, and BAGB
9	LGE1, BMSQ, BABT, BJRN, and BAGB
20	BSSG, BMSQ, BABT, BSOR, and BAGB

3. Results and Discussion

3.1. Organized Convection and GPS-PWV Jumps

Sapucci et al. (2019) [23] suggested the use of the GPS-PWV time derivative, referred to as GPS-PWV jumps, for nowcasting applications. The GPS-PWV time-derivative distribution changes as a function of the rain rate (different distribution for each rain rate tercile). The study showed the potential to extract meaningful information to nowcasting around 90 min before intense rainfall events. The methodology was carried out using GPS data collected in Outeiro station (LGE1) to check PWV jumps in a different region. The GPS station employed in this study was installed and operated during CHUVA-Belém, used by [23]. The distribution of the GPS-PWV time derivative before rainfall events, detected by the XPol radar data, is presented in Figure 2, which is included in the GPS-PWV time series (Figure 2a) and precipitation fraction in the area of 4.4 × 4.4 km centered on the GPS antenna (Figure 2b). The black bar represents precipitation fraction >20 mm h^{-1}, the dark gray bar is the fraction >35 mm h^{-1}, and the light gray bar is the fraction >50 mm h^{-1}. Similar to the analysis carried out by [23], Figure 2c shows the distribution of the GPS-PWV time derivative for the period 96 to 16 min before the maximum precipitation peak for the 12 evaluated events for different terciles of rain fraction (>35 mm h^{-1}). The four events taken into consideration in the middle tercile are indicated in Figure 2b. The four events in the other terciles are easily discerned. The same calculation was conducted for periods with rainfall events of intensities <20 mm h^{-1} including periods without observed precipitation, which is labeled in Figure 2 as "other cases".

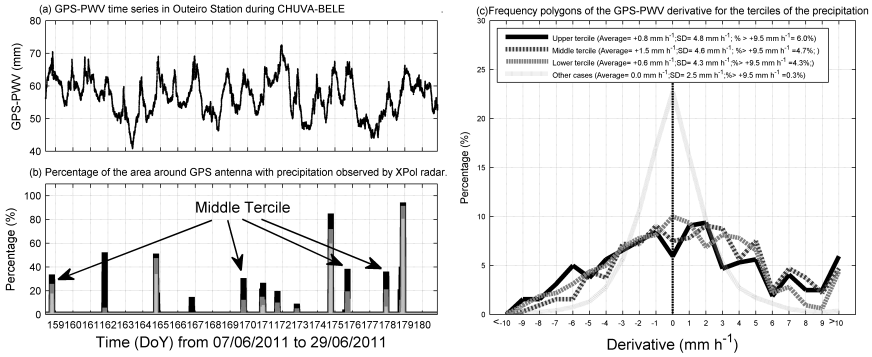

Figure 2. Frequency analysis of GPS-PWV derivative before intense precipitation in Outeiro station during CHUVA-Belém campaign: (**a**) GPS-PWV time series; (**b**) precipitation fraction from XPol radar in the area of 4.4 × 4.4 km centered on the GPS antenna, where the black bar is the fraction >20 mm/h, the dark gray bar is the fraction >35 mm/h, and the light gray bar is the fraction >50 mm/h; (**c**) frequency polygons of the GPS-PWV derivatives calculated over the period of 96 to 16 min before the maximum peak of precipitation events for different terciles and periods with rainfall events of intensities <20 mm h^{-1}, including periods without observed precipitation, labeled as "other cases".

Figure 2 does not show significant changes in the derivative histogram (c) for different precipitation intensities, as was observed in "other cases".Belém is located in the equatorial region, and PWV average value is around 55 mm. This differs greatly from the mid-latitudes, where a large change is observed in PWV before and during extreme rain events. However, even if a marked PWV jump is not observed, there is a clear difference among cases with and without rainfall. A result here that stands out is the frequency of occurrence of high GPS-PWV time derivative values (>9.5 mm h^{-1}) for all terciles evaluated. These results suggest that GPS-PWV in Belém city could be valuable for nowcasting and not only for very intense precipitation, which is the principle focus of this study, as suggested by [3], but also for nowcasting precipitation even for weak rainfall rate events. In order to explore this feature, a relationship between GPS-PWV and precipitation rates was analyzed. Our results suggest that there is actually a wide range of rainfall intensity, including weak precipitation events for organized convective systems, observed during June 2011 in Belém city.

3.1.1. Characterization of Organized Convection

Convective clouds driven by the buoyancy force are abundant in the Earth's tropical atmosphere. They vary widely in intensity and degree of organization. In some situations, these clouds are organized on the mesoscale, more precisely, in this region, as squall lines. The organized convective systems are preceded by low-level mesoscale convergence and upward motion releasing the potential instability in the temperature and moisture fields. The organized convective systems in the tropics, specifically in northern Brazil, are formed along the coast, forced by the sea breeze in the late afternoon or early evening, and propagate into the Amazonia [42].

The organized convective systems in this paper were analyzed based on the subjective method proposed by [27], which uses images from GOES satellite's infrared imagery to analyze cloud clusters' intensity and displacement. Rain cluster features in linear form were also analyzed using radar data, considering reflectivity values equal to or above 30 dBZ (CAPPI at 2 km level) over at least 111 km of length, varying in x and y. Additionally, wind profiles and thermodynamic indices (K and total-totals indexes) were employed to characterize the environmental instability associated with these organized convective systems events by radiosondes released in the airport (Figure 1) at 12 UTC (9 a.m. local

time) on 7, 9, 13, and 14 June, and in São Miguel do Guamá (Figure 1) on 24 June at 12 UTC and on 20 June at 06 UTC. Both indexes are given by the following equations [43]:

$$K = T_{850} - T_{500} + T_{d850} - Dep_{700} \quad (5)$$

$$TT = T_{850} + T_{d850} - 2T_{500} \quad (6)$$

Our subjective analysis of satellite, radar imagery, and radiosonde supports the criteria described above, and six organized convective systems were selected during the period 2–29 June 2011. Figure 3 shows satellite images and Hovmöller diagrams of the brightness temperature as a function of longitude for these six events (indicated by white arrows in the respective images), which can be divided into three different patterns, as follows:

(a) On 7 June, the convective system was organized on the mesoscale as a squall line (Figure 3a, which was also described by [25]). On 24 June (Figure 3b), the organized convective system was very similar to 7 June. On both days, the K index value was larger than 29 and total-totals index value was larger than 42. Both organized convective systems propagated 400 km inland with an average lifetime of 12 h, as cited by [27], between 16:00 UTC and 04:00 UTC, and reached a mature stage at 21 UTC (Figure 3g,h), genesis at 16 UTC, intensification at 18 UTC, and weakening at 00 UTC.There is a north wind component at 1000 hPa, 500 hPa, and 200 hPa levels (figure not shown), corroborating the results of [44], who found that a northerly component at 850 hPa perpendicular to the coast is necessary for the squall lines to enter the continent.

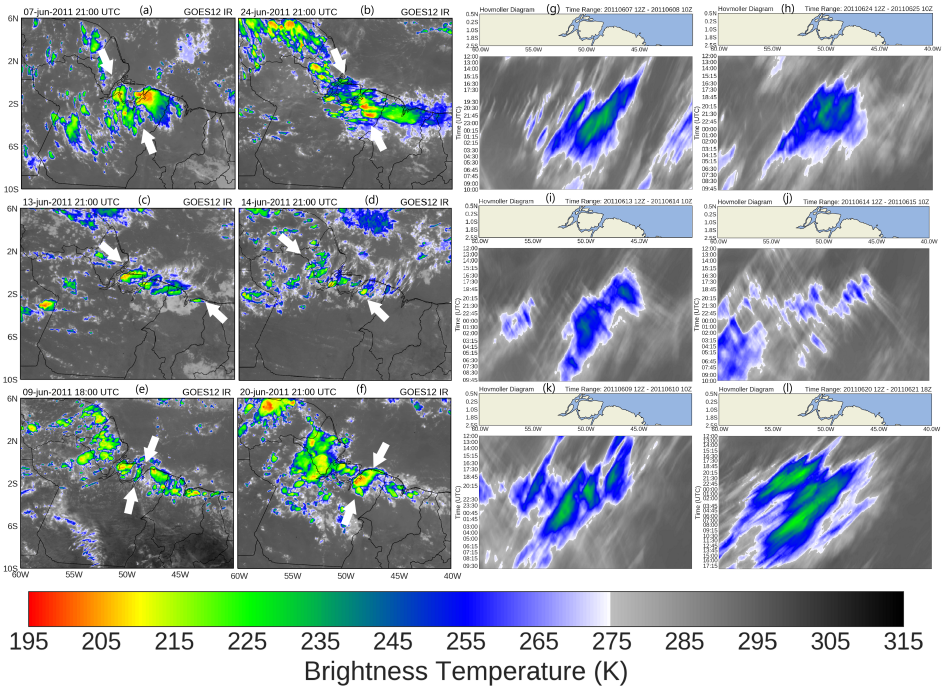

Figure 3. Satellite images (plots **a**–**f**) and Hovmöller diagrams (plots **g**–**l**) of the brightness temperature as a function of longitude for the organized convective systems observed on 7, 13, 14, 20, and 24 June, and instability microlines that occurred on 9 June.

(b) On 13 and 14 June, the convective systems were organized as coastal convection (Figure 3c,d, respectively). On both days, K index value was larger than 29 and total-totals index value was larger than 42, as cited by [43]. These systems were limited to distances less than 170 km inland, and the average lifetime was 9 h between 18:00 UTC and 03:00 UTC (Figure 3i,j) . On 14 June, the system was less intense. There is northward wind just at medium and high levels (figure not shown). These results corroborate those of [43], who also found northerly winds at a medium level.

(c) On 9 and 20 June (Figure 3e,f, respectively), the convective systems were organized along the river breeze. On 9 June, the organized convective system has an average length of 150 km and an average lifetime of 3 h, starting around 15:00 UTC over 48° W, and moving westward until reaching Marajó Bay (50° W) at 18:00 UTC (Figure 3k). On 20 June, the organized convective system has an average length of 200 km with an average lifetime of 3 h, starting at 20:30 UTC over 49° W, and moving westward also until reaching Marajó Bay (50° W) at 21:30 UTC (Figure 3l). The organized convective system was positioned along the east coast of Marajó Bay at 16 UTC on 9 June and at 20:30 UTC on 20 June. One hour later, they propagated over the Marajó Bay and in the next hour again towards the west coast of the bay (Figure 3k,l).

3.1.2. Pressure, Temperature, and GPS-PWV Time Series Behavior during Organized Convective Systems

Moisture plays an important role in the genesis and development of organized convective systems, and GPS receivers can be very useful in monitoring and predicting the location and intensity of the occurrence of these events. Ding et al. (2007) [45] described the initiation and development of a squall line by assimilation of a GPS-PWV network in a mesoscale model. In northern Brazil, Adams et al. 2015 [17] pioneered the study of convection employing a GPS-PWV network. Here, we used this 2011 Belém dense GPS-PWV network to understand the evolution of the organized convective systems characterized in the previous section.

Figure 4 shows the average and standard deviation of the diurnal cycle of GPS-PWV for the three patterns of organized convective systems and without organized convective system (hereafter, WOCS). Likewise, the diurnal cycles of GPS-PWV are displayed for each event from five ground-based GPS stations, defined in Table 2. The statistics for WOCS were calculated using all days of the evaluated period without organized convective system occurrence (including days without rainfall observed). The diurnal cycle of the five ground-based GPS stations on 7 and 24 June (Table 2) are shown using solid and dotted lines, respectively.This water vapor increase occurred on 7 June between 9 UTC and 19 UTC and on 24 June between 14 UTC and 18 UTC. The water vapor increase that was observed during the organized convective systems occurring on 13 and 14 June was also between 14 UTC to 18 UTC; however, it was more intense on 13 June than on 14 June (Figure 4c). The organized convective system appeared in the radar area around 15 UTC (Figure 3), displaying low water vapor increase (3 mm) between 11 UTC and 15 UTC on 9 June (Figure 4d). On 20 June, the organized convective system moved into the radar area at 21 UTC, exhibiting twice the water vapor increase than that observed on 9 June. Nevertheless, both organized convective systems on 9 and 20 June showed almost the same 4 h timescale of water vapor increase associated with the deep convective event. Adams et al. (2013) [13] demonstrated that 4 h prior to the GPS-PWV maximum there is a rapid increase in water vapor which they argue is reflective of water vapor convergence associated with the shallow-to-deep convection transition. Here, in these two cases, there is also intense water vapor increase 4 h prior to organized convective systems moving into the radar area.

The diurnal cycle average shows a minimum GPS-PWV at 14 UTC (11 a.m. local time) on organized convective systems and without organized convective system (hereafter, WOCS) but on 7 and 24 June, it is earlier, at 10 UTC (7 a.m. local time; Figure 4a). The GPS-PWV maximum is at 20 UTC (17 p.m. local time) on 7, 13, 14, and 24 June; it is around 22 UTC (19 p.m. local time) on 9 and 20 June, and WOCS. The maximum WOCS is associated with sea-breeze convection. GPS-PWV values on organized convective systems days are larger than on WOCS days. The GPS-PWV average at 12 UTC (9 a.m. local time when starting the heating of the atmosphere) is 6 mm (with 4 mm standard deviation) larger on 7 and 24 June than on WOCS days. The GPS-PWV average at 12 UTC is 7 mm (with 3 mm standard deviation) larger on 9 and 20 June than on WOCS days. Finally, the GPS-PWV average at 12 UTC is 1 mm (with a standard deviation of 2 mm) larger on 13 and 14

June than on WOCS. The standard deviation shows the largest value of 5 mm at 12 UTC on WOCS days. Adams et al. (2015) [17] did not find differences in GPS-PWV between convective and non-convective days in Belém at 12 UTC. However, they found that the morning CAPE is twice as large on convective days. As per [43], they found higher moisture content at 700 hPa on squall line days over the northern coast of Brazil. This behavior appears to be closely tied to the morning formation of convective lines within 30 km or so of the coast [17]. In addition, the convective lines within 30 km or so of the coast influence the GPS-PWV spreading around the five ground-based GPS stations at 11 UTC on organized convective systems. The increase in GPS-PWV on organized convective systems days is consistent with studies that consider moisture above the planetary boundary layer to be a key factor in the transition from shallow-to-deep convective clouds, which are observed during these systems [20,46,47].

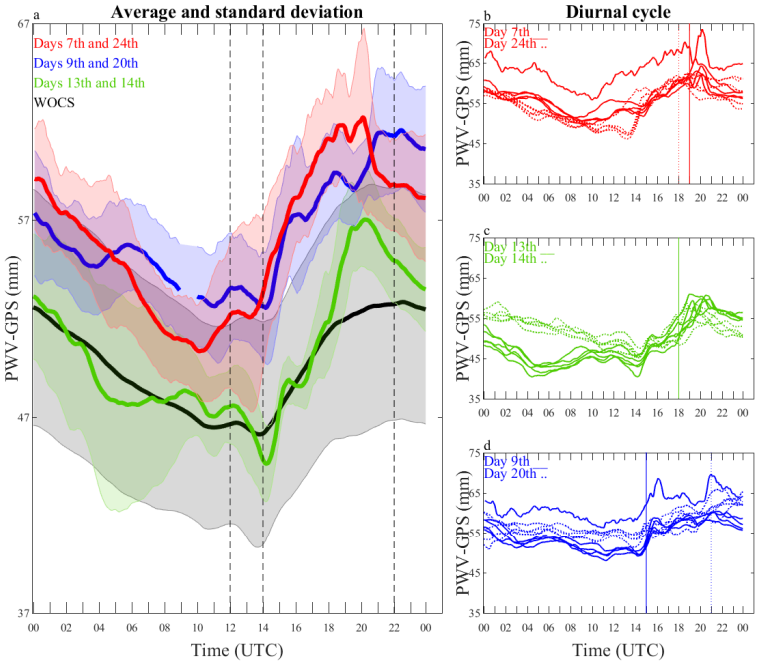

Figure 4. Diurnal cycle of GPS-PWV: (**a**) Average and standard deviation of three patterns of organized convective systems and for days without organized convective system occurrence (WOCS); (**b**) diurnal cycle of GPS-PWV of each event from 5 ground-based GPS stations, defined in Table 2 for 7 (solid lines) and 24 (dotted lines) June; (**c**) the same as (**b**), for 13 (solid lines) and 14 (dotted lines) June; (**d**) the same as (**b**), for 9 (solid lines) and 20 (dotted lines) June. Vertical lines represent the time that the organized convective systems enter into radar area.

GPS-PWV behavior is sensitive to each organized convective system; as Figure 5 shows, there are squall line passages on 7 June [25] and organized convective system on 9 June over the BJRN and BMSQ stations (respectively). The breeze front begins to enter the east coast of Pará (Figure 5a) at 16 UTC and acts as an external force for the development of a squall line. The development stage takes place at 18 UTC and some cumulus clouds begin to organize in a linear form, although not yet over the BJRN longitude. Temperature plunges to 4 °C in 1 h (from 18:15 to 19:10) and GPS-PWV also decreases rapidly to 1 mm for 20 min (between 18:45 and 19:05 UTC) (Figure 5c). This can be explained by the downdraft associated with the towers carrying denser, cooler air from the low to middle troposphere into the boundary layer. This air is relatively cooler and drier due to the melting and evaporation of precipitation particles. A portion of this convective downdraft air spreads forward and produces a gust front at the leading edge of the mesoscale system, while another portion spreads to the rear of the system [48].

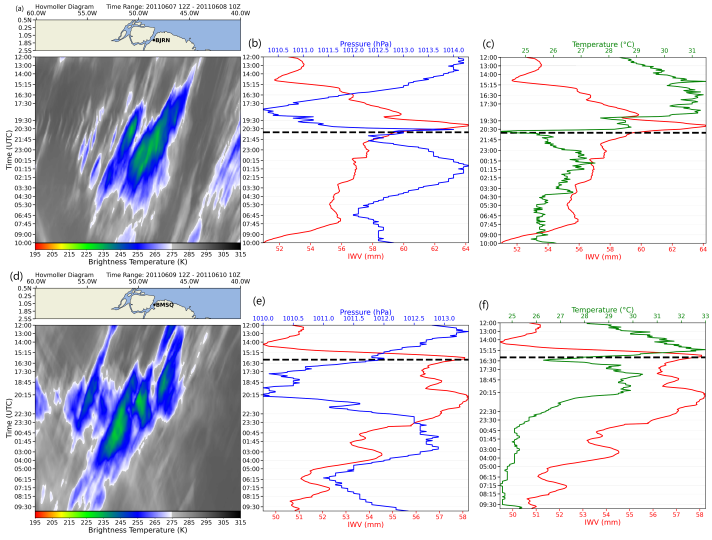

Figure 5. Hovmöller of brightness temperature (BT) (plots **a** and **d**), time series of GPS-PWV, pressure (plots **b** and **e**) and temperature (plots **c** and **f**) on 7 and 9 June observed in BJRN and BMSQ station (respectively). Dotted lines are the moment of the organized convective system passage at BJRN and BMSQ stations.

After the maximum pressure at 14 UTC (Figure 5b), it decreases to 4 hPa for 4 h until 18:10 UTC and increases to 4 hPa for 2 h 25 m until the moment of the squall line passage over BJRN station at 20:35 UTC (225 K of brightness temperature) (Figure 5a). The pressure falls followed by a small rise, indicative of the mesolow passage that is associated with the squall line. The GPS-PWV maximum at 20:05 UTC is associated with water vapor convergence and the continued formation of cloud condensate and precipitation particles. The increase in pressure during the squall line passage at 20:35 UTC is formed by the weight of precipitation in the atmospheric column. The temperature drops to 4.7 °C between 20 min before and 10 min after the squall line passage (Figure 5c). After the squall line passage, the pressure falls 2 hPa until 21:20 UTC, followed by a smooth rise, which can be explained by the mesohigh passage.

We can identify some parameters to forecast this squall line. GPS-PWV is 8 mm larger than WOCS days at 12 UTC at the BJRN station (Figure 5b). GPS-PWV convergence starts at 14:45 UTC, there are some pulses until the last minimum GPS-PWV at 19:05 UTC, and then it reaches the highest value at 20:05 UTC, followed by a strong drop. Two hours before squall line passage over the BJRN station at 20:35 UTC (225 K of brightness temperature), the pressure rises quickly to 4 hPa, followed by a drastic drop, and the temperature plunges immediately to 3 °C, followed by an increase.

The organized convective system passage over BMSQ station on 9 June at 16:05 UTC can be seen in Figure 5d. The first parameter to forecast this event is the GPS-PWV value, about 4 mm larger than WOCS days at 12 UTC at the BMSQ station (Figure 5e). The second parameter to forecast is GPS-PWV increase, which starts at 14 UTC and reaches the highest value at 15:50 UTC, followed by a drop. Temperature is the third parameter to forecast this system; we can see it plunge to 6.7 °C between 15:10 and 16:25 UTC (Figure 5f). Pressure behavior is different to the squall line; there is a pressure fall of just 1 hPa between 12:45 UTC and 15:50 UTC and a rise of 0.2 hPa at 15:55, followed by a drop (Figure 5e). We can see that the GPS-PWV value can be used to forecast both events.

3.2. The Sensitivityof GPS-PWV Jumps to Forecast Precipitation Associated with Organized Convective Systems

The sensitivityanalysis of GPS-PWV jumps to forecast precipitation associated with organized convective systems is analyzed here, based on positive pulses of the GPS-PWV (derivative > 9.5 mm h^{-1}) for higher-intensity and longer-lived events, as reported by [23]. The analysis was made by centering all the 30 time series shown in Table 2 (GPS-PWV

series on 7, 9, 13, 14, 20, and 24 June), from six events observed by five ground-based GPS receivers, on the GPS-PWV peak (time = 0) to construct the time series composite. GPS-PWV average and standard deviation, centering on the GPS-PWV maximum, of all the 30-time series used (Table 2) is presented in Figure 6. We also performed an analysis of the time lag between the GPS-PWV maximum and precipitation maximum by the relative frequency distribution of the maximum precipitation, during organized convective systems days (Table 2). From each GPS, with its latitude and longitude (Table 1), precipitation in the mean area was calculated. Among the 30 time series, 16 recorded precipitation. The histogram of precipitation maximum after GPS-PWV maximum indicates that there is a range of lag time between the GPS-PWV maximum and precipitation maximum (Figure 6). In 50.1% of the studied events, the precipitation maximum occurs between 10 and 40 min after the GPS-PWV maximum.

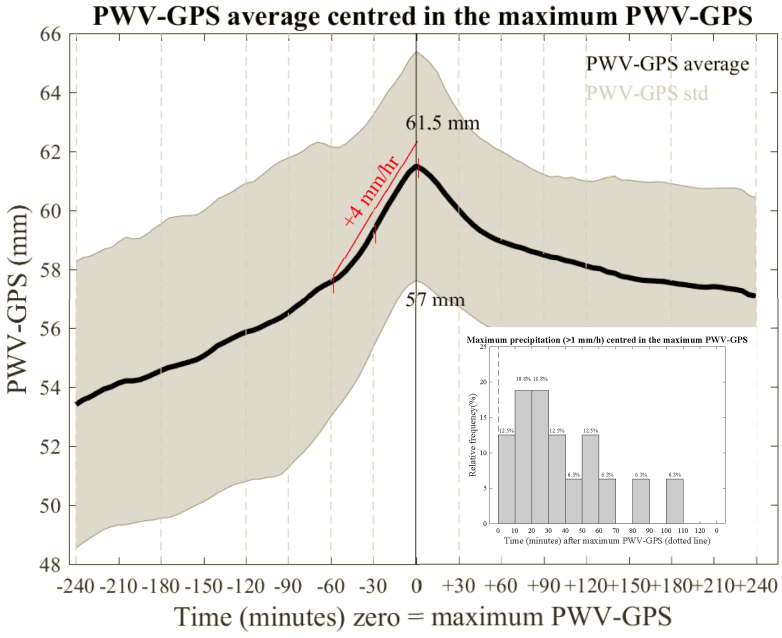

Figure 6. GPS-PWV average (black line) and standard deviation (gray shaded) of 30 time series (Table 2) centered on the GPS-PWV maximum. Relative frequency distribution of the precipitation maximum, considering at least 1 mm h^{-1}, in the area of 4.4 km × 4.4 km centered on each station (see Table 2) is shown in the time interval of 0 to 120 min after the GPS-PWV maximum.

Adopting the same methodology as that reported by [23], in which, for simplicity, only GPS-PWV data are explored as a nowcasting tool, we explored several assumptions and tested possible strategies. Our results suggest that the GPS-PWV variation rate of 4 mm h^{-1} during the period of 1 h or 30 min before the maximum peak GPS-PWV, for which this peak has a value of at least 57 mm, is able to predict the occurrence of precipitation during the organized convective systems passage (Figure 6). Variation rates found here are lower than those found by [23], as the tropical atmosphere is capable of storing a greater amount of water vapor, and therefore a change of 4 mm h^{-1} is enough to develop precipitation on organized convective systems days. Figure 6 also shows the intense convergence (8 mm) at 240 min timescale before the maximum peak GPS-PWV, and [13] also found convergence of 6 mm before deeper convection at the same timescale over Manaus city (central Amazon).

Although the GPS-PWV time series is available every 5 min, we evaluated this nowcasting index based on the CAPPI timescale, which is 10 min; consequently, this evaluation was performed for 144 points/day (24 h*60 min/10 min). In this study, the skill score of GPS-PWV jumps was assessed in terms of average precipitation (rate instantaneous per hour) over the area of 4.4 × 4.4 km, centered on each station found in Tables 2 and 3. The CAPPI values of at least 28 dBZ, which imply 2 mm h^{-1} of precipitation from the Z–R

relationship [38], were taken into consideration in the calculation of average precipitation in this area.

Table 3. Ground-based GPS stations affected by intense precipitation of above 39 dBZ or 10 mm/h on days from Table 2.

Days	Ground-Based GPS
8	LGE1
10	BMSQ
21	BAGB, BMGR
23	BSOR
30	BMSQ

The performance of this methodology was evaluated for each 10 min period when the GPS-PWV rises to 4 mm h^{-1} during a given 1 h or 30 min period in which a GPS-PWV peak of at least 57 mm occurs, followed by a drop in GPS-PWV over the next 5 min. If positive, the index is triggered, and the CAPPI product is evaluated for 120 min after this moment. If average precipitation above 2 mm h^{-1} is observed during this 120 min period, we count all points of precipitation above 0 mm until the moment that the precipitation ceases. To minimize issues of radar attenuation, if there is a point with precipitation followed by up to three readings (30 min) of missing data and immediately followed by a precipitation measurement, this period is counted as precipitating. Given that precipitation was observed, this implies that our index was successful. The same methodology was also carried out for those cases where the index was triggered without precipitation, i.e., a failure in the index. We examined all 144 points from the radar time series to see precipitation without the index being triggered, considering those cases with radar attenuation. Finally, cases without precipitation and no index triggering were calculated as follows: All data points minus cases when the index was triggered, both with and without precipitation, and when the index was not triggered but with precipitation observed. To summarize this information and evaluate the ability of this proposed forecasting methodology, a contingency table was created (Table 4), where five conventional skill parameters are presented using the equations from [49]: bias; probability of detection (POD); false alarm ratio (FAR); critical success index (CSI).

Table 4. Contingency table of the GPS-PWV jump, taking into consideration the average precipitation $\geq$2 mm h^{-1} in the area of 4.4 × 4.4 km around GPS antenna to organized convective systems (Table 2) and to precipitation from not organized convective system (above of 10 mm/h) on days listed in Table 3.

	Precipitation from Organized Convective Systems			Precipitation from Not Organized Convective Systems		
	Observed	Not Observed	Total	Observed	Not Observed	Total
Index triggered	235	80	315	5	16	21
Index not triggered	46	3959	4005	19	824	843
Total	281	4039	4320	24	840	864
Score skill	Bias		1.1 mm			0.9 mm
	POD		84%			21%
	FAR		25%			76%
	CSI		65%			13%

Table 4 shows that the index was correctly triggered in 235 points for precipitation associated with the organized convective system and not triggered in 46 radar scans. The probability detection is 84%, with a CSI of 65% and an FAR of 25%. On the other hand, the score skills for intense precipitation not associated with organized convective systems are not satisfactory. Table 4 shows the index triggered and precipitation occurring in just five radar scans (a single event) and the index triggered without precipitation for

16 radar scans from the not organized convective system. An FAR of 76% and CSI of 13% indicate that this methodology is less effective for intense precipitation events not associated with organized convective systems occurrence. In summary, this methodology has the potential for predicting precipitation observed in Belém, Brazil, associated with organized convective systems.

An open question in this GPS application is the area around the GPS antenna where the precipitation should be evaluated. Sapucci et al. (2019) [23] reported their results exploring an area of 4.4 × 4.4 km around the GPS antenna, the same used in the previous analysis here, which, although does not exactly match the cone of the GPS observation, showed the highest correlation with the rainfall area fraction of the studied events. This area is associated with the representativeness of the GPS-PWV measurement and depends on the distribution of the water vapor, but more importantly on the spatial distribution (azimuth and elevation angle) of the observed GPS satellites. We carried out a straightforward analysis of index performance with our methodology, but, in this case, modifying the representative area of the GPS cone; 2 km by 2 km, 4 km by 4 km, 8 km by km, and 10 km by 10 km centered on each station from Table 2 (Figure 7).

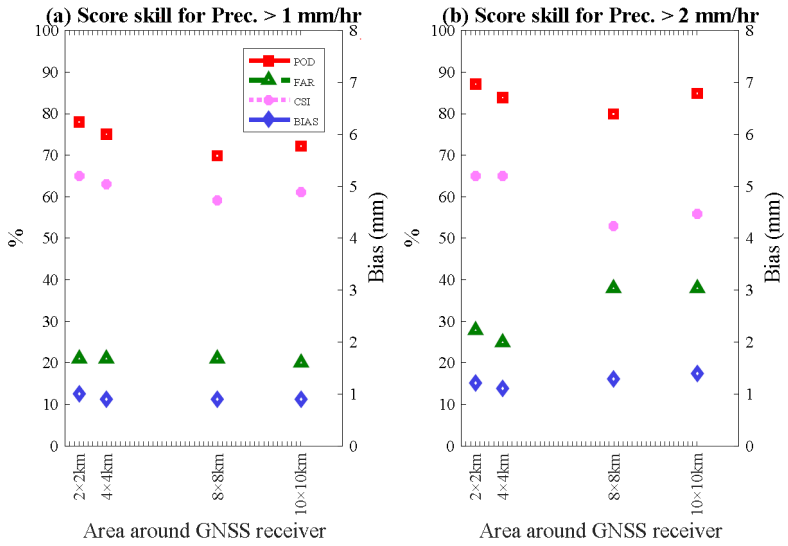

Figure 7. Skill score of the GPS-PWV jump for (**a**) average precipitation >1 mm h^{-1} and (**b**) average precipitation >2 mm h^{-1}, taking into consideration different areas around GPS antenna associated with organized convective systems .

The area of 4 × 4 km was maintained in this analysis to be compared to the results. Additionally, the performance of this methodology was assessed with a second and less intense precipitation threshold, for which the CAPPI values were at least 23 dBZ, implying 1 mm h^{-1} of precipitation from the Z–R relationship [38], that was taken into consideration in the calculation of average precipitation in these different areas. Figure 7 shows the skill score of the GPS-PWV jump for average precipitation above 1 mm h^{-1} and 2 mm h^{-1} in different areas around the GPS antenna. The results show that CSI values for average precipitation above 2 mm h^{-1} are the same for areas smaller than 4 × 4 km (CSI values of 65%). In this case, an improvement is observed in the POD index; however, the bias and FAR values are worse for a 2 × 2 km area. In areas larger than 4 × 4 km, the skill of gthe PWV jump is significantly worse (CSI values about 50%), which is strongly impacted by an increase of FAR values (38%). These results indicate that the large area around the GPS antenna includes rainfall far away from the antenna location, which may not be associated with the local increase in PWV, consequently decreasing the skill of GPS-PWV for the nowcasting tool. On the other hand, smaller areas around the GPS antenna present similar skill to 4 × 4 km, but restrict the ray action of GPS, requiring a very dense network without real necessity. These results corroborate the conclusion reported by [23], which indicates

that the PWV jump presents the better skill to predict the precipitation observed in an area of 4 × 4 km around the GPS antenna.

The scores in Figure 7 show that the performance of the methodology is similar to average precipitation above 1 mm h^{-1} and 2 mm h^{-1} and 4 × 4 km area (CSI of 62% and 65%, FAR of 20% and 25%, respectively). The methodology is penalized when the index has been triggered and average precipitation is above 2 mm h^{-1}, mainly for 8 × 8 km and 10 × 10 km areas (CSI values are bigger and FAR are smaller in precipitation below 2 mm h^{-1}), in which an increase of area contributes to penalizing the methodology. This result indicates that the method is sensitive not only to average precipitation above 2 mm h^{-1}, but that it also can be useful for average precipitation above 1 mm h^{-1}. This is an interesting result because it increases the range of applications of this tool for a larger range of precipitation events.

The performance of the methodology is studied in two events: (a) an event when the index was triggered and there was average precipitation of 2.5 mm h^{-1} in the 4.4 × 4.4 km area around the BMSQ station on 9 June (Figure 8); (b) an event when the index was not triggered and there was precipitation of 16.31 mm h^{-1} in the 4.4 × 4.4 km area around the BAGB station on 7 June (Figure 9).

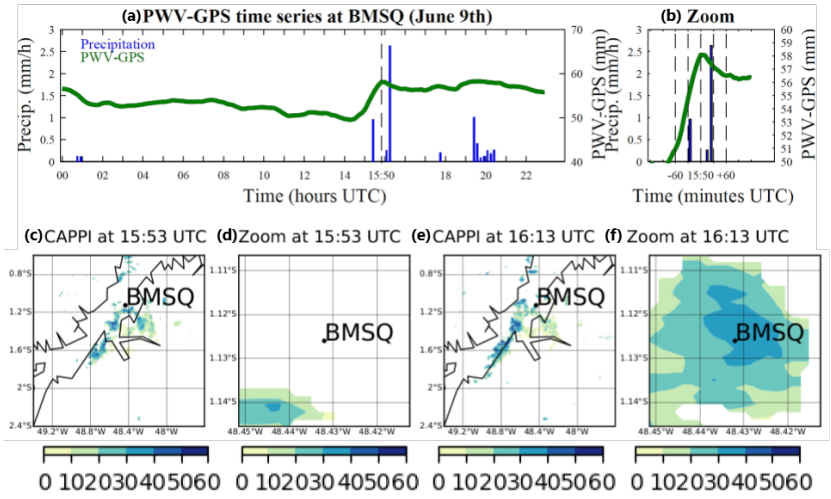

Figure 8. GPS-PWV and precipitation observed over the BMSQ station: (**a**) time series; (**b**) the zoom at GPS-PWV maximum (dotted line); (**c**) average CAPPI value at 2 km level in total radar area at 13:53 UTC; (**d**) zoom at the 4.4 km × 4.4 km area around the BMSQ station at 13:53 UTC; (**e**) the same as (**c**) at 13:13 UTC, and (**f**) the same as (**d**) at 16:13 UTC.

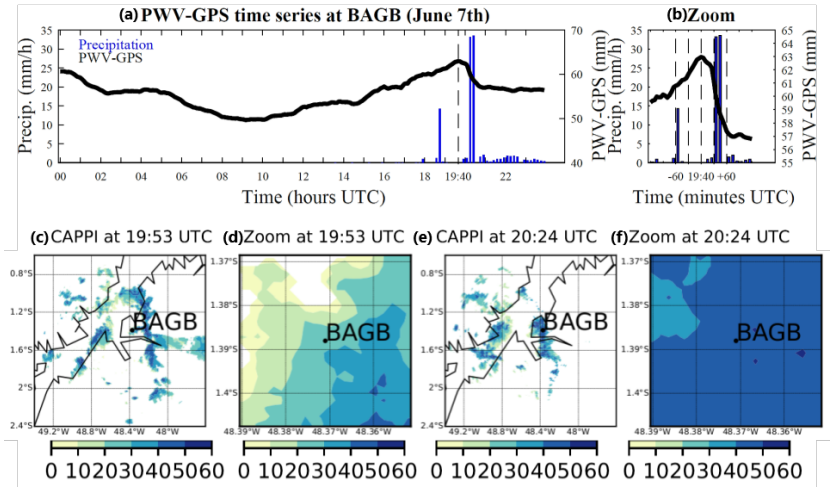

Figure 9. The same as Figure 8 for the BAGB station on 7 June.

Figure 8a shows the first indication of an organized convective system day at 12 UTC when the GPS-PWV at the BMSQ station displays 50.7 mm (4 mm greater than days without organized convective system). From 12 UTC to 14:15 UTC, GPS-PWV varies between stability and dropping. It reaches a minimum of 49.45 mm at 14:15 UTC; 1 h after that minimum value, the GPS-PWV shows an increase of 4.5 mm. However, the criterion is not applied, given that the GPS-PWV continues to increase until 15:50. At 15:55, the GPS-PWV registers the first drop, so the criterion is triggered at 15:50 UTC. The difference between the GPS-PWV maximum and the GPS-PWV 30 min before the GPS-PWV maximum is 3.3 mm, and this would be enough to trigger the criterion. The difference between the GPS-PWV maximum and the GPS-PWV 60 min before the GPS-PWV maximum is also sufficient to trigger the criterion, at 7.1 mm. The radar image at 15:53 UTC (Figure 8c,d) shows that the organized convective system is positioned along the east coast of Marajó Bay, registering an average precipitation of 0.48 mm in the 4.4 × 4.4 km area around the BMSQ station. The precipitation maximum (2.5 mm h^{-1}) observed by the radar occurs at 16:13 UTC (Figure 8e,f).

Figure 9a indicates an organized convective system day at 12 UTC, when the GPS-PWV at the BAGB station is 52.6 mm (6 mm greater than days without organized convective system). From 12 UTC to 14:30 UTC, GPS-PWV varies between stability and drop. It reaches a minimum of 53.29 mm at 14:30 UTC, and at 16:35 UTC it reaches a high value followed by a drop, but not enough to trigger the criterion. From 16:50 UTC, the GPS-PWV increases again until reaching the GPS-PWV maximum at 19:40 UTC, followed by a fall. However, the criterion is not triggered. The difference between the GPS-PWV maximum and the GPS-PWV 30 min before the GPS-PWV maximum is 1.3 mm, and between the GPS-PWV maximum and the GPS-PWV 60 min before the GPS-PWV maximum, it is 2.1 mm. Although the index was not triggered, the organized convective system is observed in the radar image at 19:53 (Figure 9c,d) in a northwest–southeast direction, very close to the BAGB station and already registering average precipitation of 1.13 mm in the 4.4 × 4.4 km area around the BAGB station. The precipitation maximum observed by the radar occurred at 20:24 UTC (Figure 9e,f) and registered significant precipitation of 16.31 mm in the 4.4 × 4.4 km area around the BAGB station. In this event, where there is a strong GPS-PWV increase after 10 UTC, it appears that a small PWV rise is enough to be associated with strong precipitation.

This study indicates that observing the GPS-PWV value at 12 UTC may be valuable for forecasting, due to the high GPS-PWV in the atmosphere in organized convective systems. Observing the 5 minute PWV values, likewise, may be of use to forecasters. When the index is triggered (GPS-PWV variation rate of 4 mm h^{-1} during a period of 1 h or 30 min before the maximum peak GPS-PWV (at least 57 mm), followed by a fall), this would indicate to the forecaster that there is an 84% chance of average precipitation above 2 mm h^{-1} in the 4.4 × 4.4 km area around the GPS antenna.

4. Conclusions

This research assessed the sensitivityof GPS-PWV jumps to precipitation events that occurred during organized convective systems in Belém in the Brazilian state of Pará. The results showed that a specific behavior in the GPS-PWV time series anticipates the occurrence of these events. A methodology was proposed, taking into consideration only GPS-PWV time series to predict the precipitation associated with organized convective systems. The results show that a rise to 4 mm h^{-1} in a period of an hour or 30 min before maximum peak GPS-PWV (at least 57 mm) indicates the precipitation occurrence. The performance of this methodology was evaluated using data from 30 time series from the different GPS receivers. The skill score obtained was 84% for the probability of detection and 25% for false alarm rate of forecasting average precipitation above 2 mm h^{-1}. A second analysis, taking into consideration the precipitation observed in different areas around the GPS antenna, showed that the area 4.4 × 4.4 km (as reported by [23]) provided the best skill of this methodology for precipitation events evaluated. When average precipitation above

1 mm h^{-1} was explored, a decrease in the skill score of this methodology was observed, which reached 75% for the probability of detection; however, the false alarm rate showed an improvement of 5% (FAR of 20%). The reason for the probability of detection degradation is due to the correlation between the index not being triggered and fewer events for average precipitation above 2 mm h^{-1} than for average precipitation above 1 mm h^{-1}. On the other hand, the false alarm rate was improved because of the index triggered, and more precipitation was observed above 1 mm h^{-1} than above 2 mm h^{-1}. This is an important result that indicates that this methodology can be explored, not only for intense precipitation, as suggested by [23], but also for the moderate precipitation associated with organized convective systems in Belém city, thereby expanding this method's range of application within this region.

Author Contributions: Conceptualization and methodology were conduced by T.B.C. and L.F.S.; GPS data processing and validation estimates were provide by L.F.S.; Precipitation data processing and analysis were done by C.E.; formal analysis and investigation were provided by T.B.C.; writing original draft preparation was done by T.B.C. and L.F.S., writing—review and editing, L.A.T.M. and D.K.A.; Supervision L.F.S.; Project administration and funding acquisition, Machado. L. All authors have read and agreed to the published version of the manuscript.

Funding: Financial support was provided by Coordination of Improvement of Higher Education Personnel (CAPES) (Finance Code 001), National Council for Scientific and Technological Development (CNPq), São Paulo Research Foundation, (FAPESP; grant process numbers 2009/15235-8, 2015/14497-0, 2015/03804-9, and 2019/12015-9), Contractual Instrument of the Thematic Network of Geotectonic Studies CT-PETRO (PETROBRAS). Thanks to the National Institute for Space Researches (INPE) (grant number 600289299), which provided the GPS receivers used in the dense network.

Data Availability Statement: The data base used in this study is available at site http://ftp.cptec.inpe.br/chuva/belem/experimental/ and additional information can be accessed at CHUVA project website http://chuvaproject.cptec.inpe.br/portal/ftp.jsp.

Acknowledgments: Thanks to the members of the CHUVA team involved in the data collection by XPol radar during the CHUVA Vale experiment in Belém PA. Special thanks to Thiago Souza Biscaro, responsible for radar data processing, and Lucas Amarantes, responsible for GPS data processing.

Conflicts of Interest: The authors declare no conflicts of interest.

References

1. Bevis, M.; Businger, S.; Herring T.A.; Rocken, C.; Anthes, R.A.; Ware, R.H. GPS meteorology: Remote sensing of atmospheric water vapor using the global positioning system. *J. Geophys. Res.* **1992**, *97*, 15787–15801. [CrossRef]
2. Rocken, C.; Ware R.; Van Hove, T.; Solheim, F.; Alber, C.; Johnson, J.; Bevis, M.; Businger, S. Sensing atmospheric water vapor with the global positioning system. *Geophys. Res. Lett.* **1993**, *20*, 2631–2634. [CrossRef]
3. Rocken, C.; Van Hove, T.; Johnson, J.; Solheim, F.; Ware, R.; Bevis, M.; Chiswell, S.; Businger, S. TGPS/STORM—GPS Sensing of Atmospheric Water Vapor for Meteorology. *J. Atmos. Ocean Technol.* **1995**, *12*, 468–478. [CrossRef]
4. Bonafoni, S.; Riccardo, B. The usefulness of the Global Navigation Satellite Systems (GNSS) in the analysis of precipitation events. *Atmos. Res.* **2016**, *167*, 15–23. [CrossRef]
5. Cucurull, L.; Vandenberghe, F.; Barker, D.; Vilaclara, E.; Rius, A. Three-dimensional variational data assimilation of ground-based GPS ZTD and meteorological observations during the 14 December 2001 storm event over the western Mediterranean sea. *Mon. Weather Rev.* **2004**, *132*, 749–763. [CrossRef]
6. Gutman, S.; Sahm, S.; Benjamin, S.; Schwartz, B.; Holub, K.; Stewart, J.; Smith, T. Rapid Retrieval and Assimilation of Ground Based GPS Precipitable Water Observations at the NOAA Forecast Systems Laboratory: Impact on Weather Forecasts. *J. Meteorol. Soc. JPN* **2004**, *82*, 351–360.
7. Bennitt, G.V.; Jupp, A. Operational assimilation of GPS zenith total delay observations into the Met Office numerical weather prediction models. *Mon. Weather Rev.* **2012**, *140*, 2706–2719. [CrossRef]
8. Risanto, C.B.; Castro, C.L.; Arellano, A.F.; Moker, J.M.; Adams, D.K. The Impact of Assimilating GPS Precipitable Water Vapor in Convective-Permitting WRF-ARW on North American Monsoon Precipitation Forecasts over Northwest Mexico. *Mon. Weather Rev.* **2021**, *149*, 3013–3035.
9. Jerrett, D.; Nash, J. Potential uses of surface based GPS water vapour measurements for meteorological purposes. *Phys. Chem. Earth Part A Solid Earth Geod.* **2001**, *26*, 457–461. [CrossRef]
10. Mazany, R.A.; Businger, S.; Gutman, S.I.; Roeder, W. A Lightning Prediction Index that Utilizes GPS Integrated Precipitable Water Vapor. *Weather Forecast.* **2002**, *17*, 1034–1047.

11. De Haan, S.; Barlag, S.; Baltink, H.K.; Debie, F.; Van der Marel, H. Synergetic use of GPS water vapor and Meteosat images for synoptic weather forecasting. *J. Appl. Meteorol.* **2004**, *43*, 514–518. [CrossRef]
12. Kursinski, E.R.; Bennett, R.A.; Gochis, D.; Gutman, S.I.; Holub, K.L.; Mastaler, R.; Minjarez Sosa, C.; Minjarez Sosa, I.; Van-Hove, T. Water vapor and surface observations in northwestern Mexico during the 2004 NAME Enhanced Observing Period. *Geophys. Res. Lett.* **2008**, *35*, 4–9. [CrossRef]
13. Adams, D.K.; Gutman, S.I.; Holub, K.L.; Pereira, D.S. GNSS observations of deep convective time scales in the Amazon. *Geophys. Res. Lett.* **2013**, *40*, 2818–2823. [CrossRef]
14. Benevides, P.; Catalao, J.; Miranda, P.M.A. On the inclusion of GPS precipitable water vapour in the nowcasting of rainfall. *Nat. Hazards Earth Syst. Sci.* **2015**, *15*, 2605–2616. [CrossRef]
15. Bastin, S.; Champollion, C.; Bock, O.; Drobinski, P.; Masson, F. On the use of GPS tomography to investigate water vapor variability during a Mistral/sea breeze event in southeastern France. *Geophys. Res. Lett.* **2005**, *32*. [CrossRef]
16. Miranda, P.M.A.; Mateus, P. Improved GNSS Water Vapor Tomography With Modified Mapping Functions. *Geophys. Res. Lett.* **2022**, *49*, e2022GL100140. [CrossRef]
17. Adams, D.K.; Fernandes, R.M.S.; Holub, K.L.; Gutman, S.I.; Barbosa, H.M.J.; Machado, L.A.T.; Calheiros, A.J.P.; Bennett, R.A.; Kursinski, E.R.; Sapucci, L.F.; et al. The amazon dense gnss meteorological network a new approach for examining water vapor and deep convection interactions in the tropics. *Bull. Am. Meteorol. Soc.* **2015**, *96*, 2151–2165. [CrossRef]
18. Adams, D.K.; Barbosa, H.M.J.; Gaitan de los Rios, K.P. A Spatiotemporal Water Vapor–Deep Convection Correlation Metric Derived from the Amazon Dense GNSS Meteorological Network. *Mon. Weather Rev.* **2017**, *145*, 279–288. [CrossRef]
19. Muller, C.J.; Back, L.E.; O'Gorman, P.A.; Emanuel, K.A.T. A model for the relationship between tropical precipitation and column water vapor. *Geophys. Res. Lett.* **2009**, *36*, L16804. [CrossRef]
20. Holloway, C.E.; Neelin, J.D. Moisture vertical structure, column water vapor, and tropical deep convection. *J. Atmos. Sci.* **2009**, *66*, 1665–1683. [CrossRef]
21. Madhulatha, A.; Rajeevan, M.; Venkat-Ratnam, M.; Bhate, J.; Naidu, C.V. Nowcasting severe convective activity over southeast India using ground-based microwave radiometer observations. *J. Geophys. Res. Atmos.* **2013**, *118*, 1–13. [CrossRef]
22. De Haan, S. Measuring Atmospheric Stability with GPS. *J. Appl. Meteorol. Climatol.* **2006**, *45*, 467–475. [CrossRef]
23. Sapucci, L.F.; Machado, L.A.T.; Souza, E.; Campos, T. Global Positioning System precipitable water vapor (GPS-PWV) jumps before intense rain events: A potential application to nowcasting. *Meteorol. Appl.* **2019**, *26*, 49–63. [CrossRef]
24. Guerova, G.; Dimitrova, T.; Georgiev, S. Thunderstorm Classification Functions Based on Instability Indices and GNSS IWV for the Sofia Plain. *Remote Sens.* **2019**, *11*, 2988. [CrossRef]
25. Machado, L.A.T.; Silva Dias, M.A.F.; Morales, C.; Fisch, G.; Vila, D.; Albrecht, R.; Goodman, S.J.; Calheiros, A.J.P.; Biscaro, T.; Kummerow, C.; et al. The Chuva Project: How Does Convection Vary across Brazil? *Bull. Am. Meteorol. Soc.* **2014**, *95*, 1365–1380. [CrossRef]
26. Garstang, M.; Massie, H.L.; Halverson, J.; Greco, S.; Scala, J. Amazon coastal squall lines. Part I: Structure and kinematics. *Mon. Weather Rev.* **1994**, *122*, 608–622. [CrossRef]
27. Cohen, J.C.P.; Silva Dias, M.A.F.; Nobre, C.A. Environmental Conditions Associated with Amazonian Squall Lines: A Case Study. *Mon. Weather Rev.* **1995**, *123*, 3163–3174. [CrossRef]
28. Lyard, F.; Lefevre, F.; Letellier, T.; Francis, O. Modelling the global ocean tides: Modern insights from FES2004. *Ocean Dynam.* **2006**, *56*, 394–415. [CrossRef]
29. Schmid, R.; Steigenberger, P.; Gendt, G.; Ge, M.; Rothacher, M. Generation of a consistent absolute phase-center correction model for GPS receiver and satellite antennas. *J. Geod.* **2007**, *81*, 781–798. [CrossRef]
30. Montenbruck, O.; Schmid, R.; Mercier, F.; Steigenberger, P.; Noll, C.; Fatkulin, R.; Kogure, S.; Ganeshan, A.S. GNSS satellite geometry and attitude models. *Adv. Space Res.* **2015**, *56*, 1015–1029. [CrossRef]
31. Boehm, J.; Werl, B.; Schuh, H. Troposphere mapping functions for GPS and very long baseline interferometry from European Centre for Medium-Range Weather Forecasts operational analysis data. *J. Geophys. Res.* **2006**, *111*, 1–9. [CrossRef]
32. Davis, J.L.; Herrinch, T.A.; Shapiro, I.I.; Rollers, A.E.E.; Elglered, G. Geodesy by radio interferometry: Effects of atmospheric modeling errors on estimates of baseline length. *Radio Sci.* **1985**, *20*, 1593–1607. [CrossRef]
33. Bevis, M.; Businger, S.; Chiswell, S.; Herring, T.A.; Anthes, R.A.; Rocken, C.; Ware, R.H. GPS Meteorology: Mapping Zenith Wet Delays onto Precipitable Water. *J. Appl. Meteorol. Climatol.* **1994**, *33*, 379–386. [CrossRef]
34. Sapucci, L.F. Evaluation of Modeling Water-Vapor-Weighted Mean Tropospheric Temperature for GNSS-Integrated Water Vapor Estimates in Brazil. *J. Appl. Meteorol. Climatol.* **2014**, *53*, 715–730. [CrossRef]
35. Testud J.; Le Bouar, E.; Obligis, E.; Ali-Mehenni, M. The Rain Profiling Algorithm Applied to Polarimetric Weather Radar. *J. Atmos. Ocean Technol.* **2000**, *17*, 332–356. [CrossRef]
36. Calheiros, A.J.P.; Machado, L.A.T. Cloud and rain liquid water statistics in the CHUVA campaign. *Atmos. Res.* **2014**, *144*, 126–140. [CrossRef]
37. Park, S.-G.; Bringi, V.N.; Chandrasekar, V.; Maki, M.; Iwanami, K. Correction of Radar Reflectivity and Differential Reflectivity for Rain Attenuation at X Band. Part I: Theoretical and Empirical Basis. *J. Atmos. Ocean Technol.* **2005**, *22*, 1621–1632. [CrossRef]
38. Marshall, J.S.; Palmer, W.K.M. The distribution of raindrops with size. *J. Meteorol.* **1948**, *5*, 165–166. [CrossRef]
39. Vila, D.A.; Machado, L.A.T.; Laurent, H.; Velasco, I. Forecast and Tracking the Evolution of Cloud Clusters (ForTraCC) Using Satellite Infrared Imagery: Methodology and Validation. *Weather Forecast.* **2008**, *23*, 233–245. [CrossRef]

40. Madhulatha, A.; Tsmohan, M.; Thampi, S.B. Observational aspects of tropical mesoscale convective systems over southeast India. *J. Earth Syst. Sci.* **2020**, *129*, 1–26. [CrossRef]
41. Salio, P.; Nicolini, M.; Zipser, E.J. Mesoscale Convective Systems over Southeastern South America and Their Relationship with the South American Low-Level Jet. *Mon. Weather Rev.* **2007**, *135*, 1290–1309. [CrossRef]
42. Anselmo, E.M.; Machado, L.A.T.; Schumacher, C.; Kiladis, G.N. Amazonian mesoscale convective systems: Life cycle and propagation characteristics. *Int. J. Climatol.* **2021**, *41*, 3968–3981. [CrossRef]
43. Oliveira, F.P.; Oyama, M.D. Antecedent Atmospheric Conditions Related to Squall-Line Initiation over the Northern Coast of Brazil in July. *Weather Forecast.* **2015**, *30*, 1254–1264. [CrossRef]
44. Kousky, V.E. Diurnal rainfall variation in northeast Brazil. *Mon. Weather Rev.* **1980**, *108*, 488–498. [CrossRef]
45. Ding, J.; Yang, Y.; Ye, Q.; Huang, Y.; Ma, X.; Ma, L.; Guo, Y.R. Moisture analysis of a squall line case based on precipitable water vapor data from a ground-based GPS network in the Yangtze River Delta. *Adv. Atmos. Sci.* **2007**, *24*, 409–420. [CrossRef]
46. Derbyshire, S.H.; Beau, I.; Bechtold, P.; Grandpeix, J.Y.; Piriou, J.M.; Redelsperger, J.L.; Soares, P.M.M. Sensitivity of moist convection to environmental humidity. *Q. J. R. Meteorol. Soc.* **2004**, *130*, 3055–3079. [CrossRef]
47. Zhang, Y.; Klein, S.A. Mechanisms affecting the transition from shallow to deep convection over land: Inferences from observations of the diurnal cycle collected at the ARM southern great plains site. *J. Atmos. Sci.* **2010**, *67*, 2943–2959. [CrossRef]
48. Gamache, J.F.; Houze, R.A., Jr. Mesoscale air motions associated with a tropical squall line. *Mon. Weather Rev.* **1982**, *10*, 118–135. [CrossRef]
49. Wilks, D. Statistical methods in the atmospheric sciences. In *Statistical Methods in the Atmospheric Sciences*, 3rd ed.; Academic Press: Cambridge, MA, USA, 1995.